TiO_2 nanotube arrays on silicon substrate for on-chip supercapacitors

Gang Li[1,2], Jian Li[1,2] Tingyu Li[1] and Kaiying Wang[1, 3, *]

[1] *School of Information and Computer Science, TaiYuan University of Technology, Shanxi, 030024, China*

[2] *MicroNano System Research Center, Key Lab of Advanced Transducers and Intelligent Control System Taiyuan University of Technology,Taiyuan, China*

[3] *Department of MicroSystems, University of South-Eastern Norway, Horten 3184, Norway*

*Corresponding Author: E-mail: Kaiying.Wang@usn.no, Tel: + 47 3100 9317

Journal of Power Sources, 425, 39-43.
https://doi.org/10.1016/j.jpowsour.2019.03.120

Abstract: With the ever-increasing development of micro/nano electronic systems, the need grows for smart and efficient on-chip energy-storage devices with high-performance and long lifetime. In this work, for the first time we demonstrate TiO_2 nanotube arrays (TNTAs) as a high-surface-area scaffold to construct 3D nanostructured electrode on planar silicon substrate for on-chip supercapacitors. The ordered TNTAs are grown by directly anodizing Ti film sputtered on planar silicon substrate. The TNTAs are then electrochemically reduced to enhance their electrical conductivity. The reduced TNTAs exhibit both extremely low series resistance of 5.7 Ω and optimal specific capacitance of 5.6 $mF \cdot cm^{-2}$ at 0.05 $mA \cdot cm^{-2}$, which is 5 times higher than that of pristine TNTAs on silicon substrate. Furthermore, the reduced TNTAs are used as scaffolds to support MnO_2 nanoparticles by electrochemical deposition. The MnO_2 decorated TNTAs show maximum specific capacitance 20.6 $mF \cdot cm^{-2}$ (volumetric specific capacitance of 103 $F \cdot cm^{-3}$) at 0.05 $mA \cdot cm^{-2}$ as well as excellent cycling stability with 82.1% capacitance retained after 3000 charge-discharge cycles. Such integration of silicon based TNTAs might open up new opportunities to construct 3D nanostructured electrodes, free of expensive and complicated MEMS technologies, for high-performance on-chip supercapacitors.

Key words: TiO_2 nanotube, manganese oxide, anodic oxidation, on-chip supercapacitor

1. Introduction

Supercapacitors (SCs, or electrochemical capacitors), owing to their high power density, robust lifetimes, rapid charging capabilities[1, 2], have been applied in various areas[3], such as automotive and microelectronics industries, as well as space exploration, biomedical research and healthcare[4]. With recent advances in the design and fabrication of microelectronic devices based on silicon (Si)[5], small devices with low power consumption[6] are expected. In this context, SCs are developed for on-chip micro-supercapacitors (MSCs) [7] to fit into the application field of microelectronic devices [8]. However, low energy density and high cost[9] are the bottleneck hindering their applications.

In the last few years, many efforts for on-chip MSCs have been devoted to the pursuit of superior performance[10, 11], mainly focusing on mass loading[12] of active materials [13]. There are two major approaches for increasing the on-chip capacitance: The first approach is to construct 3D Si nanostructure based on bulk (subtracting silicon from silicon substrate) and surface silicon micromachining technologies. For instance, Lu et al. fabricated a composite TiN/Si nanorod (NR) electrode with an area capacitance of 1.55 $mF \cdot cm^{-2}$ at the scan rate of 2 mV/s based on bulk silicon technologies[14]. Dubal et al. deposited MnO_2 on SiNWs to form a 3D core-shell electrode with a high area capacitance of 13 $mF \cdot cm^{-2}$ based on surface micromachining technologies [15]. Furthermore, 3D Si nanowires[16]/nanorods[17] coated with active materials such as RuO_2[18], PANI[19], PPy[20], TiN[14], CNTs[21] have been widely developed for on-chip SCs. The second approach is to directly construct 3D nanostructured electrodes on the silicon surface. For instance, Hsia et al. reported a 3D carbon interdigitated microelectrode derived from the photolithography and carbonization of SU-8 photoresist on silicon substrate, which yields a specific area capacitance of 1.5-3.5 $mF \cdot cm^{-2}$ and a specific volumetric capacitance of 15-35 $F \cdot cm^{-3}$ [22]. To further enhance the area capacitance, 3D photoresist-derived microstructures coated with RuO_2/CNT [23] and MnO_2/CNT [24] have been developed for high-performance on-chip SCs. Although the above approaches have achieved high specific area capacitance, these 3D nanostructured electrodes still suffer from the complicated and expensive MEMS technologies such as silicon etching[25] (DRIE, ICP) and thin film deposition (ALD, CVD) technologies.

To obtain practical and high-power on-chip SCs, creating a high specific surface area film[26] to break

the limitation is a necessary requirement for on-chip SCs [10]. The ordered TNTAs film with high aspect ratio holds great promise to serve as SCs electrodes [12, 27]. However, previous studies have reported that

the TNTAs thin films applied to SCs were fabricated on Ti foil substrates, which could not be integrated with Si based MEMS technologies for on-chip SCs [28]. The aim of this work is to construct 3D TNTAs as a high-surface-area scaffold by directly anodizing Ti film sputtered on planar silicon substrate for on-chip SCs. The TNTAs will be further treated with a facile self-doping process[29] to enhance the electrical conductivity. Then, we demonstrate the TNTAs as high-surface-area scaffolds by loading MnO_2 nanoparticles through electrochemical deposition to form high-performance 3D nanostructured composite electrodes[30] free of expensive and complicated MEMS technologies. The detailed structure, morphological characteristic and electrochemical properties of the electrode will be characterized and discussed.

2. Experimental method

Titanium thin films (1.2 μm thick) were deposited on n-type silicon (100) wafer ((Fig. 1a-b)) by D.C. magnetron sputtering. The purity of Ti target is 99.5%. The silicon substrate was heated to 500°C during Ti sputtering deposition. Argon gas was pumped into chamber as plasma source. Argon gas flow rate was set to keep pressure at 0.93 Pa in the chamber. After sputtering, the wafer was cooled down to room temperature in vacuum to minimize the formation of titanium dioxide. Furthermore, TNTAs were grown on silicon substrate through anodic oxidation experiments. Titanium film (1.2μm thick) was firstly deposited by D.C. magnetron sputtering on the cleaned n-type silicon (100) wafer to form Ti film/Si wafer as illustrated in Fig. 1a and 1b. Prior to the anodization, the Ti film/Si wafers were ultrasonically cleaned in acetone, isopropanol and alcohol for 10 min and then were rinsed with distilled water and dried in air. The Ti film/Si wafers as the anode were electrochemically anodized at 25℃ in the electrolyte, consisting of 5.0 vol% distilled water, 0.5 wt% NH_4F and ethylene glycol. The TNTAs growth is a result of dynamic balance of field oxide formation and chemical dissolution of TiO_2 due to the action of fluoride ions during the whole anodization [31]:

$$Ti + 2H_2O \rightarrow TiO_2 + 4H^+ + 4e^- \quad (1)$$

$$TiO_2 + 4H^+ + 6F^- \rightarrow TiF_6^{2-} + 2H_2O \quad (2)$$

Then, the as-formed TNTAs (Fig. 1c) were thoroughly and ultrasonically washed in ethylene glycol and subsequently in ethanol until white floccus is detached from the surface, and then annealed at 450℃ in ambient atmosphere for 2 h to attain anatase crystal. After the anodic oxidation, electrochemical reduction

technique was adopted for fabricating the reduced TNTAs (r-TNTAs). The experiment was carried out in a two-electrode system that the TNTAs films were used as cathode and the carbon rod as anode. The pristine TNTAs were reduced in a 0.5M Na_2SO_4 aqueous solution at 20 V for a period of 5min (Fig. 1d). The r-TNTAs are prepared via electrochemical reduced pristine TNTAs film at suitable negative potential using aqueous electrolyte (Na_2SO_4). Semiconducting behavior of TiO_2 is altered by an introduction of oxygen vacancies (Ti^{3+} sites) to optimize the electrochemical performance ($Ti^{4+} + e^- + H^+ \rightarrow Ti^{3+}H^+$) [32, 33]. It is believed that electrochemical reduction of TiO_2 could be a wise way to break the restrictions of conductivity. The r-TNTAs film serves as current collector and scaffolds for loading MnO_2. We used r-TNTAs as current collector to support MnO_2 nanoparticles(r-TNTAs@MnO_2) for advancing the capacitive performance, MnO_2 can be viewed as a replaceable choice[34] to RuO_2 for the remarkable advantages of high theoretical specific capacitance, low toxicity, low cost and environmental friendliness.

The loading of MnO_2 nanoparticles were realized by electrochemical deposition technique (Fig. 1e). The TNTAs were soaked in 0.1M manganese acetate for 6 h to accumulate Mn^{2+} in the inner side of nanotubes. A three-electrode system was assembled by employing the Si/TiO_2 sample, Pt mesh, and SCE as working, counter, and reference electrode, respectively. We performed electrochemical deposition at 0.9 V (vs. SCE) in 0.25M $MnSO_4$+0.25M Na_2SO_4 aqueous electrolyte solution, potentiostatic pulse mode was employed to deposit MnO_2 on the pristine TNTAs and r-TNTAs respectively. The mass loading of MnO_2 was controlled ($Mn^{2+}+2H_2O=MnO_2+4H^++2e^-$)[35] by repeating the pulsing period for 13 cycles. After the electrochemical deposition process, the electrode sample was mildly washed with deionized water and dried at 80°C.

The morphology of all-prepared samples TiO_2/Ti/Si after electrochemical processes was characterized using a scanning electron microscope (SEM, JSM-7001F, and Japan). X-ray diffraction (XRD) was used to investigate phase formation of the samples (Rigaku D/Max-2400). The electrochemical properties of individual electrode at different stage and the assembled Si/r-TNTAs@MnO_2 electrode of MSC were investigated by cyclic voltammetry (CV), electrochemical impedance spectra (EIS) and galvanostatic charge-discharge (GCD) test employing an electrochemical workstation (ZAHNER, Germany). Tests of single electrode were carried out in a conventional three-electrode cell. The as-prepared samples, platinum mesh and Ag/AgCl were used as working, counter and reference electrode, respectively. A 0.5 M Na_2SO_4 neutral aqueous solution is used as electrolyte. The cycling stability of the Si/r-TNTAs@MnO_2 samples

was investigated by GCD test performed up to 3000 cycles at a current density of 0.2mA·cm^{-2}. All the electrochemical tests described above were carried out at 25 ℃.

3. Result and discussion

Fig 2 shows the SEM images and XRD patterns of TNTAs before and after depositing MnO_2 nanoparticles. The morphology of highly ordered pristine TNTAs is shown in Fig. 2a. The diameter of the nanotubes is about 115 nm with an average wall thickness of ~9 nm, which can be seen in the enlarged view in Fig. 2b. The nanotubes length is about 2.00 μm, as shown in the cross-sectional view of Fig. 2c, which is obviously thicker than the sputtered titanium film. The sputtered titanium film on silicon substrate is not fully reacted after the anodic oxidation because there is still residual titanium layer (~ 150 nm) as shown in Fig. 2c. The un-reacted titanium layer could serve as a bridge to connect the anodic layer and silicon substrate. The morphology of r-TNTAs does not show any significant change after the electrochemical reduction and deposition, e.g. tube broken, nanotubes faults, as shown in Fig. 2(d, e). After depositing MnO_2 nanoparticles, the cross-sectional view Fig. 2f shows that the MnO_2 clusters are distributed along the TNTAs, where average tube inner diameter is reduced to ~95 nm. The element mapping (red box marked in Fig. 2(d, f)) presents distribution of manganese elements at the top view (Fig. 2g) and cross-section (Fig. 2h) of TNTAs, which show a uniform deposition of manganese element.

X-ray diffraction technique was used to characterize the material composition and crystal phases of the samples. Fig. 2i depicts the XRD patterns of Si/TNTAs, Si/r-TNTAs and Si/r-TNTAs@MnO_2 performed from 2-theta 20° to 80°. All peaks for both pristine and r-TNTAs are indexed to anatase and brookite because of the relatively low process temperature, except for the peaks at 25.6° originated from Si substrates. The peak at 28.7° corresponds to the manganese dioxide phase confirming the expected formation of MnO_2. The XRD pattern also shows the presence [36] of MnOOH, Mn_3O_4, and Mn_2O_3.

Electrochemical measurements have been carried out to evaluate the electrochemical performance of Si/r-TNTAs@MnO_2 electrode. The electrochemical behavior based on the Si/r-TNTAs@MnO_2 in Na_2SO_4 neutral aqueous electrolyte has been studied by CV, GCD, and EIS curves. Fig. 3 presents the performance of Si/TNTAs, Si/r-TNTAs, Si/TNTAs@MnO_2, and Si/r-TNTAs@MnO_2 electrodes. The comparative CV curves recorded at 50 mV·s^{-1} are shown in Fig. 3a, it can be seen that the electrochemical response of pristine Si/TNTAs is relatively small at the voltage window (0-0.6V), suggesting poor capacitive behavior.

Clearly, the CV curve of r-TNTAs electrode exhibits a larger integrated area and higher current response than that of pristine TNTAs electrode, indicating an improved capacitive behavior after the electrochemical reduction. The expansion of the integrated area is attributed to the enhanced carrier density and increased density of hydroxyl group. Furthermore, the CV curve for r-TNTAs electrode is close to an ideal rectangular shape with no identifiable redox peaks, which is typical characteristic of double-layer capacitance [37]. In contrast, Si/TNTAs@MnO_2 sample shows a weaker response compared with Si/r-TNTAs@MnO_2 electrode, which is due to the poor electrical conductivity of MnO_2 formed on the pristine TNTAs film. The result implies that the electrochemical reduction technology is an efficient method improving the electrical conductivity and the capacity. Furthermore, it is worth noting that the Si/r-TNTAs@MnO_2 electrode in Na_2SO_4 electrolyte provides enhanced capacitive performance (about 20 times higher) as compared to the pristine Si/TNTAs electrode. The nearly rectangular CV response reflects the continuous and reversible faradaic reaction of MnO_2. The CV curves of Si/r-TNTAs@MnO_2 with different scan rate deviates from the ideal rectangle (Fig. 3b) due to the impurity of manganese oxide.

Representative GCD curves of different samples obtained at a current density 0.05 $mA \cdot cm^{-2}$ are presented in Fig. 3c. For the pristine Si/TNTAs, the discharge time is 13 s and thus a relatively low area specific capacitance of 1.1 mF cm^{-2} is obtained from the discharge curve. The r-TNTAs samples exhibits longer discharge time (67s) than that of Si/TNTAs sample, showing an area capacitance of 5.6 mF cm^{-2} at the same current density. The discharge time of Si/TNTAs@MnO_2 samples is 72 s, the electrode presents better capacitive performance, and a relatively low areal specific capacitance 6.0 mF cm^{-2} is obtained. Fig. 3d shows the GCD curves of Si/r-TNTAs@MnO_2 electrodes collected at different current density. The discharge time increases with the decrease of current density, and the areal specific capacitance decreases with increasing current density due to the limited ion diffusion. At the lowest current density (0.05 $mA \cdot cm^{-2}$), the Si/r-TNTAs@MnO_2 electrode delivers an average areal capacitance of 20.6 $mF \cdot cm^{-2}$ (discharge time is 247s) with the volumetric specific capacitance 103 $F \cdot cm^{-3}$, which is significant higher than that of 3D nanostructured electrodes based on Si nanowires/rods[14] coated with MnO_2 [25], RuO_2[38] and photolithography and carbonization of photoresist [22]. The GCD curves with nearly isosceles triangle represent the superior performance of manganese oxide and an ideal supercapacitor charge storage

mechanism in this voltage range.

The Nyquist plots are presented in Fig. 3e to assess the resistance and capacitance of different

electrodes in the frequency range of 100 kHz and 100 mHz (vs. Ag/AgCl) at a bias voltage of 5 mV. All EIS spectra displayed similar shapes, which comprise of a small arc in the high frequency region and a straight line in the low frequency region. The intercept of the small arc on real axis are related to equivalent series resistances (ESR, R_S), which are associated with ionic resistance of electrolytic solution, internal resistance of nanostructure and the contact resistance (resistance of the barrier layer) between nanostructure and current collector[25]. The R_s of Si/TNTAs, Si/r-TNTAs, Si/r-TNTAs@MnO_2 and Si/TNTAs@MnO_2 are found to be 13.0 Ω, 5.7 Ω, 7.5 Ω and 32.2 Ω, respectively. The semi-circular arcs correspond to charge transfer resistance (CTR, R_{ct}) at electrode/electrolyte interface. The R_{ct} of Si/TNTAs, Si/r-TNTAs, Si/r-TNTAs@MnO_2 and Si/TNTAs@MnO_2 are 15.5 Ω, 2.5 Ω, 10.5 Ω and 12.1 Ω, respectively. The decrease in *Rs* and *Rct* for Si/r-TNTAs@MnO_2 compared to Si/TNTAs electrode indicates its higher electronic conductivity[39]. In the low frequency range, the slope of straight line corresponds to the Warburg diffusive resistance inside the electrode (Z_w), which is related to the capacitive performance. Both Si/r-TNTAs and Si/r-TNTAs@MnO_2 show a near-vertical line at low frequency, indicating the good capacitive behavior and capacitive behavior because of the decreased electrical conductivity[40], which are obtained by introduction of oxygen vacancy states (Ti^{3+}) of the electrodes.

The cycling stability is one of the most important factors of supercapacitor electrode. Fig. 3f shows the cycling stability of the optimal Si/r-TNTAs@MnO_2 electrode by repeating GCD cycles at a current density of 0.2 mA·cm^{-2} up to 3000 cycles. After 3000 cycles, the specific capacitance decreased from 20.58 mF·cm^{-2} to 16.89 mF·cm^{-2}, demonstrating the excellent cycling stability[41] with the retention of capacitances over 82.1% after 3000 cycles. The little variation in cycling stability between titanium-based [32, 33] and silicon-based nanotube films further indicates high cycling stability of the electrodes.

4. Conclusion

In summary, TNTAs high-surface-area scaffolds are integrated with silicon substrate for on-chip MSCs to power microelectronics. The highly ordered TNTAs have been achieved by directly anodizing Ti film sputtered on silicon substrate. The Si/r-TNTAs electrode exhibits a typical characteristic of double-layer capacitance, which is attributed to the enhanced electrical conductivity of TNTAs by using a facile electrochemically reduced method. Furthermore, we demonstrate that the high conductive on-chip TNTAs

are used as a good scaffold to support active materials. In comparison with Si/TNTAs@MnO_2 electrode

without electrochemically reduction, the Si/r-TNTAs@MnO_2 electrode further exhibits higher areal capacitance of 20.6 $mF \cdot cm^{-2}$, volumetric capacitance of 103 $F \cdot cm^{-3}$ as well as excellent long-term stability with capacitance retention of 82.1% after 3000 cycles. The integrated TNTAs and enhanced conductivity concept will provide great opportunities to develop cheap and high-performance MSCs.

Acknowledgement

This research was supported by the National Natural Science Foundation of China (61674113, 51622507, and 61471255), Natural Science Foundation of Shanxi Province, China (2016011040), and Scientific and Technological Innovation Programs of Higher Education Institutions in Shanxi Province, China (2016138).

Reference

[1] P. Huang, C. Lethien, S. Pinaud, K. Brousse, R. Laloo, V. Turq, M. Respaud, A. Demortière, B. Daffos, P.L. Taberna, B. Chaudret, Y. Gogotsi, P. Simon, Science, 351 (2016) 691-695.
[2] M. Beidaghi, Y. Gogotsi, Energy & Environmental Science, 7 (2014) 867.
[3] W. Xu, J. Lu, W. Huo, J. Li, X. Wang, C. Zhang, X. Gu, C. Hu, Nanoscale, 10 (2018) 14304-14313.
[4] J. Jiang, Y. Li, J. Liu, X. Huang, C. Yuan, X.W. Lou, Advanced materials, 24 (2012) 5166-5180.
[5] M. Ahmed, B. Wang, B. Gupta, J.J. Boeckl, N. Motta, F. Iacopi, Journal of The Electrochemical Society, 164 (2017) A638-A644.
[6] H. Hu, Z. Pei, C. Ye, Energy Storage Materials, 1 (2015) 82-102.
[7] Z.S. Wu, K. Parvez, S. Li, S. Yang, Z. Liu, S. Liu, X. Feng, K. Mullen, Advanced materials, 27 (2015) 4054-4061.
[8] D. Pech, M. Brunet, P.-L. Taberna, P. Simon, N. Fabre, F. Mesnilgrente, V. Conédéra, H. Durou, Journal of Power Sources, 195 (2010) 1266-1269.
[9] P. Huang, M. Heon, D. Pech, M. Brunet, P.-L. Taberna, Y. Gogotsi, S. Lofland, J.D. Hettinger, P. Simon, Journal of Power Sources, 225 (2013) 240-244.
[10] C. Shen, X. Wang, W. Zhang, F. Kang, Journal of Power Sources, 196 (2011) 10465-10471.
[11] G. Wang, L. Zhang, J. Zhang, Chemical Society reviews, 41 (2012) 797-828.
[12] W. Fang, O. Chyan, C. Sun, C. Wu, C. Chen, K. Chen, L. Chen, J. Huang, Electrochemistry Communications, 9 (2007) 239-244.
[13] X. Wang, Y. Yin, X. Li, Z. You, Journal of Power Sources, 252 (2014) 64-72.
[14] P. Lu, P. Ohlckers, L. Müller, S. Leopold, M. Hoffmann, K. Grigoras, J. Ahopelto, M. Prunnila, X. Chen, Electrochemistry Communications, 70 (2016) 51-55.
[15] D.P. Dubal, D. Aradilla, G. Bidan, P. Gentile, T.J. Schubert, J. Wimberg, S. Sadki, P. Gomez-Romero, Scientific reports, 5 (2015) 9771.
[16] S. Ortaboy, J.P. Alper, F. Rossi, G. Bertoni, G. Salviati, C. Carraro, R. Maboudian, Energy & Environmental Science, 10 (2017) 1505-1516.
[17] P. Lu, E. Halvorsen, P. Ohlckers, L. Müller, S. Leopold, M. Hoffmann, K. Grigoras, J. Ahopelto, M. Prunnila, X. Chen, Electrochimica Acta, 248 (2017) 397-408.
[18] X. Wang, Y. Yin, C. Hao, Z. You, Carbon, 82 (2015) 436-445.
[19] J. Chen, Z. Xia, H. Li, Q. Li, Y. Zhang, Electrochimica Acta, 166 (2015) 174-182.
[20] P. Zhu, T. Cai, Sensors and Actuators B: Chemical, 213 (2015) 202-208.
[21] P. Lu, L. Müller, M. Hoffmann, X. Chen, Nano Energy, 41 (2017) 618-625.
[22] B. Hsia, M.S. Kim, M. Vincent, C. Carraro, R. Maboudian, Carbon, 57 (2013) 395-400.
[23] Y. Yin, International Journal of Electrochemical Science, (2017) 3883-3906.
[24] S. Jiang, T. Shi, D. Liu, H. Long, S. Xi, F. Wu, X. Li, Q. Xia, Z. Tang, Journal of Power Sources, 262 (2014) 494-500.

[25] C.J. Raj, M. Rajesh, R. Manikandan, J.Y. Sim, K.H. Yu, S.Y. Park, J.H. Song, B.C. Kim, Electrochimica Acta, 247 (2017) 949-957.
[26] Z.S. Wu, K. Parvez, X. Feng, K. Mullen, Nature communications, 4 (2013) 2487.

[27] M. Zhou, A.M. Glushenkov, O. Kartachova, Y. Li, Y. Chen, Journal of the Electrochemical Society, 162 (2015) A5065-A5069.
[28] K.N. Chappanda, Y.R. Smith, S.K. Mohanty, L.W. Rieth, P. Tathireddy, M. Misra, Nanoscale Research Letters, 7 (2012) 388.
[29] X. Lu, M. Yu, G. Wang, T. Zhai, S. Xie, Y. Ling, Y. Tong, Y. Li, Advanced materials, 25 (2013) 267-272.
[30] W.C. Huo, X.L. Liu, Y.S. Yuan, N. Li, T. Lan, X.Y. Liu, Y.X. Zhang, Frontiers in chemistry, 6 (2018) 661.
[31] K. Přikrylová, J. Drbohlavová, V. Svatoš, I. Gablech, L. Kalina, Z. Pytlíček, R. Hrdý, J. Hubálek, Monatshefte für Chemie - Chemical Monthly, 147 (2016) 943-949.
[32] H. Zhou, Y. Zhang, The Journal of Physical Chemistry C, 118 (2014) 5626-5636.
[33] X. Lu, G. Wang, T. Zhai, M. Yu, J. Gan, Y. Tong, Y. Li, Nano letters, 12 (2012) 1690-1696.
[34] W. Xu, Z. Jiang, Q. Yang, W. Huo, M.S. Javed, Y. Li, L. Huang, X. Gu, C. Hu, Nano Energy, 43 (2018) 168-176.
[35] Z. Zeng, X. Long, H. Zhou, E. Guo, X. Wang, Z. Hu, Electrochimica Acta, 163 (2015) 107-115.
[36] S. Zhu, L. Li, J. Liu, H. Wang, T. Wang, Y. Zhang, L. Zhang, R.S. Ruoff, F. Dong, ACS nano, 12 (2018) 1033-1042.
[37] N. Li, X. Huang, H. Zhang, Y. Li, C. Wang, ACS applied materials & interfaces, 9 (2017) 9763-9771.
[38] W. Zheng, Q. Cheng, D. Wang, C.V. Thompson, Journal of Power Sources, 341 (2017) 1-10.
[39] H.R. Barai, M.M. Rahman, S.W. Joo, Journal of Power Sources, 372 (2017) 227-234.
[40] X. Shi, Z. Zeng, C. Liao, S. Tao, E. Guo, X. Long, X. Wang, D. Deng, Y. Dai, Journal of Alloys and Compounds, 739 (2018) 979-986.
[41] W. Xu, J. Wan, W. Huo, Q. Yang, Y. Li, C. Zhang, X. Gu, C. Hu, Chemical Engineering Journal, 354 (2018) 1050-1057.

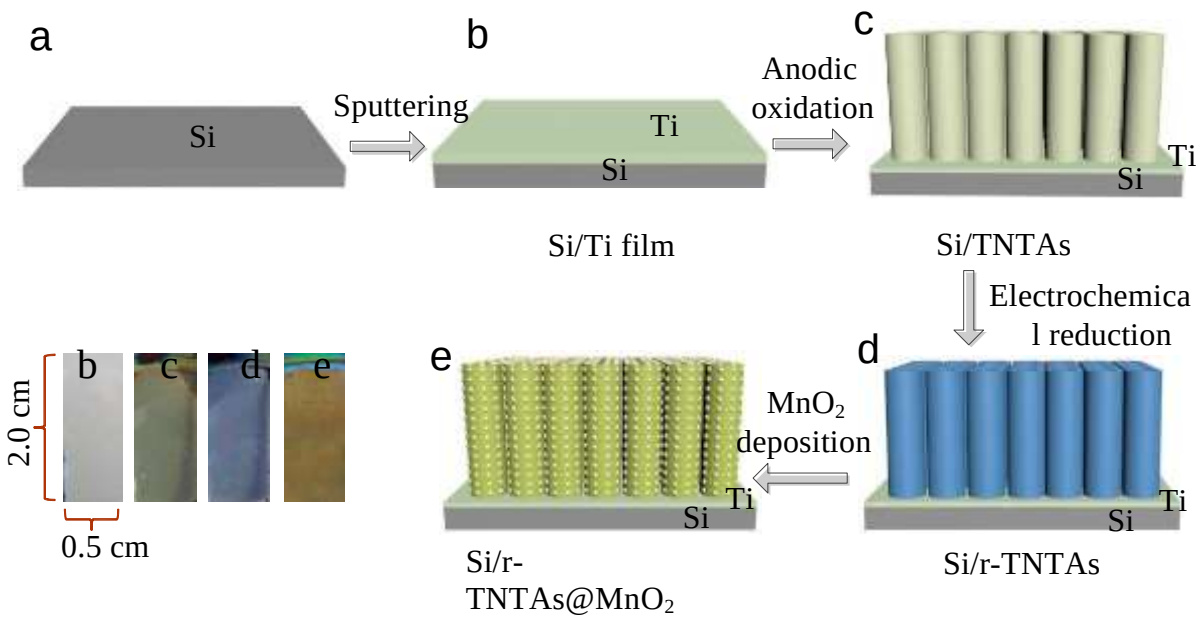

Fig 1 Schematic illustration of the fabrication process of Si/r-TNTAs@MnO_2 electrode: a) Si wafer, b) Ti sputtering, c) Anodization, d) Electrochemical reduction, e) MnO_2 deposition.

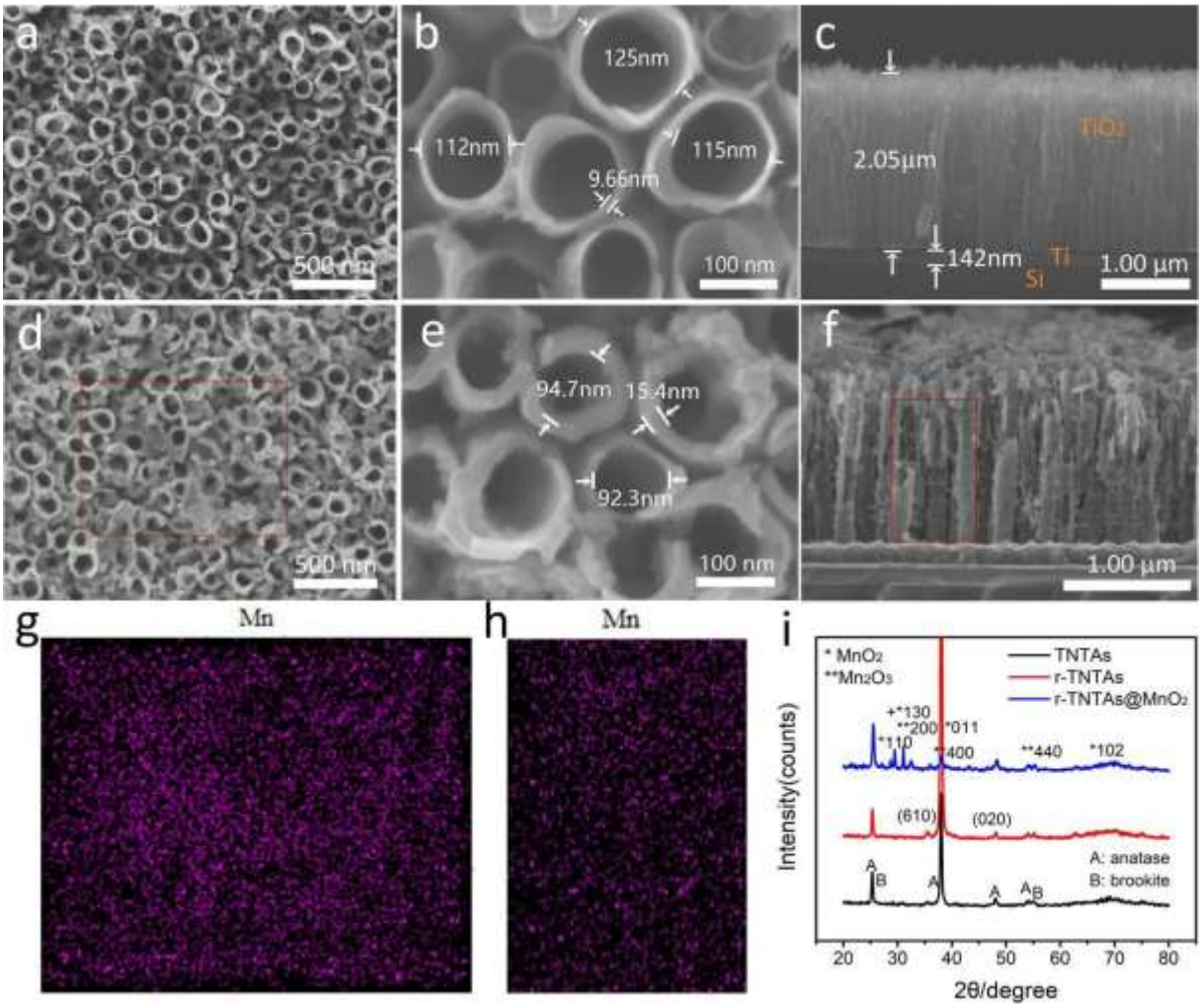

Fig 2 SEM images: (a) Top view of the pristine TNTAs, (b) High-magnification image of the pristine TNTAs, (c) Cross-sectional image of the pristine TNTAs, (d) Top view of r-TNTAs@MnO_2, (e) High-magnification image of r-TNTAs@MnO_2, (f) Cross-sectional image of r-TNTAs@MnO_2, (g) Elemental mapping of the rectangle area in Fig.2d, (h) Elemental mapping of the rectangle area in Fig.2f, (i) XRD

patterns.

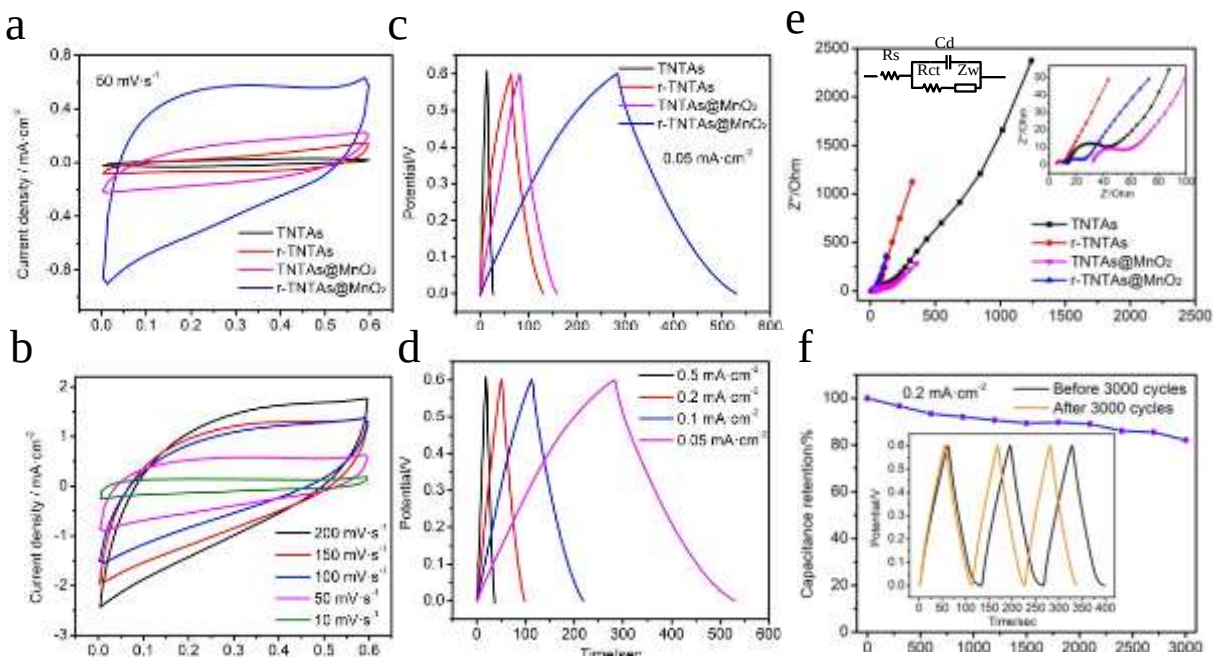

Fig 3 (a) CV curves of different samples collected at a scan rate of 50mV/s, (b) CV curves of Si/r-TNTAs@MnO_2 sample collected at different scan rates, (c) GCD curves of the different samples collected at 0.05mA/cm^2, (d) GCD curves of Si/r-TNTAs@MnO_2 collected at different current densities, (e) Nyquist plots, (f) Cycling stability of Si/r-TNTAs@MnO_2 sample.